



Experimental study of the effect of crack distribution on the failure mechanism of sandstone specimens based on inclination angles and number of parallel flaws

Jiewen Pang · Yongliang He · Qiaoyun Han ·
Deyang Ba · Xiaoyuan Sun

Received: 24 September 2023 / Accepted: 9 March 2024
© The Author(s) 2024

Abstract Discontinuous joints are prevalent in engineered rock masses and play a significant role in the stability of the rock mass. This study aims to analyze the impact of the inclination angle and number of prefabricated flaws on the crack evolution and failure pattern of sandstone specimens. Uniaxial compression tests, along with acoustic emission technology and digital image technology, were employed to monitor and analyze the effects. The findings indicate that: (1) With the increase in the flaw inclination angle, the damage mode of the specimen transitions from tensile to compressive-shear failure. The localized high-strain region on the surface of the specimen predicts the propagation path for the formation of macroscopic cracks. (2) When the number of prefabricated flaws is small, the flaws mainly expand through tensile wing cracks. As the number of flaws

increases, the inner flaw tip does not produce cracks. Instead, the failure of the entire specimen occurs along the direction of the outer flaw's tensile wing crack, with the inner flaw running through it. (3) The winged tensile crack is the first crack to appear in all rock samples, regardless of the flaw initiation angles. Finally, the stress intensity factor at the crack tip under uniaxial compression conditions, without considering the closure effect, was expressed based on fracture mechanics theory. The crack initiation angle was then calculated. The results of the theoretical calculation of the initiation angle were found to be consistent with the test results. These research findings can serve as theoretical references and provide insights into the failure mechanisms of cracked rocks and the development of disaster control methods in rock engineering.

J. Pang (✉) · Y. He · X. Sun
School of Safety and Emergency Management
Engineering, Taiyuan University of Science
and Technology, Taiyuan 030024,
People's Republic of China
e-mail: pjwfanfan@126.com

Q. Han
School of Civil Engineering, Hunan University
of Science and Technology, Xiangtan 411201,
People's Republic of China

D. Ba
China Construction Sixth Engineering Bureau Corp., Ltd,
Tianjin 300000, People's Republic of China

Article Highlights

- The increase in the number of flaws of sandstone specimens reduces the ultimate propagation length of the wing crack, leading to through failure and a reduced load carrying capacity of the specimen at lower compressive stresses.
- As the inclination angle of the sandstone specimen flaw increases, the failure mode of the specimen transitions from shear to compressive failure. During the initial stage of loading, a high-strain region emerges around the flaw. As loading continues, a

localized high-strain region develops on the surface of the specimen, indicating the path along which a macroscopic crack may form.

- When there are only a few flaws in the sandstone specimens, the flaws primarily spread through tensile wing cracks. As the number of flaws increases, the inner flaw does not generate tip cracks. Instead, the failure of the entire specimen occurs along the direction of the tensile wing crack of the outer prefabricated flaw, with the inner flaw extending through the specimen, resulting in an anti-tensile crack.
- Among the sandstone specimens with all flaw inclination angles, the winged tensile crack was the first crack to appear. Based on the principle of fracture mechanics, the expression of the stress intensity factor at the tip of the crack under uniaxial compression conditions without considering the closure effect was given, the crack initiation angle was calculated, and the theoretical calculation of the initiation angle was basically consistent with the test results.

Keywords Discontinuous joints · Failure process · Crack propagation · Acoustic emission (AE) · Digital image correlation techniques

1 Introduction

The engineering rock mass is subjected to long-term crustal movement, engineering excavation, and various types of load disturbances. Its interior contains numerous joints, cracks, and structural surfaces. These flaws are primarily developed due to external loads, causing them to nucleate in localized areas of failure. Subsequently, the flaws further localize and eventually lead to the propagation of macroscopic crack coalescence. This phenomenon gives rise to common disasters such as tunnel collapse, mine subsidence, rock slope instability, landslides, and poses a significant threat to human life and property (Chang et al. 2018; Zhang and Zhou 2020; Lei et al. 2020; Han et al. 2020). Therefore, conducting research on the effect of crack parameters on the crack propagation and failure patterns of rock materials under uniaxial compression conditions is crucial for evaluating the extent of rock failure and holds great engineering significance.

In recent years, there have been numerous experimental studies conducted by scholars on rock materials with prefabricated flaws using indoor testing methods. The mechanical properties and failure patterns of cracked rocks have been studied in two main ways: firstly, by creating different geometrical arrangements of flaws on intact rock specimens, and secondly, by creating different geometrical arrangements of flaws on specimens of rock-like materials. For instance, Yang et al. (2022) conducted triaxial compression tests on cracked granite specimens to examine the effects of rock bridge angle and circumferential pressure on the mechanical properties and damage modes of granite specimens. They also analyzed the internal microscopic damage characteristics of granite specimens using CT scanning technology. Similarly, Li et al. (2005a) created flaws on rock specimens through the drilling and cutting method and studied the process of crack propagation, identifying two types of nascent cracks. Huang et al. (2022) proposed five crack propagation paths and corresponding damage modes based on their study of rock crack propagation rules. Reisi et al. (2015) conducted experimental studies on cracked sandstone specimens and identified and proposed nine crack types to study crack propagation and damage patterns. Zhou et al. (2014) described the characteristics of five crack types using specimens containing double and multiple cracks. Similar studies have also been conducted by Zhou et al. (2019a), Liu et al. (2021), Wang et al. (2023), and Alneasan and Behnia (2022), Alneasan et al. (2022, 2023). These research findings provide a theoretical basis for understanding the fracture mechanism of engineering rock masses.

Due to the challenges and expenses associated with obtaining and fabricating flawed rock specimens, researchers have conducted numerous studies to investigate crack propagation patterns and specimen damage by using different types of rock-like materials to fabricate flawed specimens. Initially, some studies explored the crack propagation pattern under compressive loading using glass specimens (Hoek and Bieniawski 1965). Bobet and Einstein (1998) used gypsum materials to fabricate double-flaw specimens for experimental studies, aiming to observe crack misalignment, secondary crack sprouting, and coalescence patterns, and analyze the relationship between specimen failure patterns and the distribution of prefabricated flaws. Zhao et al. (2018) examined the

crack propagation process of gypsum samples containing two parallel flaws through uniaxial compression tests. While compression tests using glass or gypsum materials effectively describe the compression damage characteristics of crystalline connection type rock materials, they still have limitations in explaining the compression damage characteristics of cemented connection type rock materials. Therefore, some studies have proposed the use of cement mortar materials to simulate the deformation failure characteristics of cracked rock. Yang et al. (2021) investigated the correspondence between crack propagation and stress–strain curves by creating flawed specimens with cement mortar. Cao et al. (2015) utilized cement mortar specimens to simulate the crack initiation and agglomeration behavior of brittle rock materials. The combination of coarse and fine aggregates in the cement mortar better aligns with the characteristics of engineered rock masses. Similar studies have also been conducted by Meysam et al. (Lak et al. 2019a, 2019b; Mohebbi et al. 2017; Abdollahipour and Marji 2020; Fu et al. 2022; Abdollahipour et al. 2016).

With the advancement of technology, auxiliary monitoring means in the laboratory can be utilized to study the failure characteristics and processes of cracked rocks in more detail from a microscopic perspective. Currently, the commonly used methods for this purpose are acoustic emission monitoring techniques (AE) (Modiriasari et al. 2017; Morgan and Einstein 2017; Zhang et al. 2019) and digital image correlation techniques (DIC) (Ji et al. 2016; Munoz and Taheri 2017; Liu et al. 2015). Eberhardt et al. (Eberhardt et al. 1998) employed acoustic emission techniques to investigate the damage process of granite and found that significant acoustic emission events or a sudden increase in acoustic emission characteristic parameters often correspond to the initiation of microcracks. Lin et al. (2013) analyzed the damage process of the specimen by examining the changing law of the strain field on the specimen surface. Moreover, the rapid development of modern computer technology has made numerical simulation methods a popular approach for studying rock mechanics problems. Some commonly used software for this purpose includes RFPA (Wong and Lin 2015; Wang et al. 2014), PFC (Sarfarazi et al. 2014; Huang et al. 2019), and UDEC (Debecker and Vervoort 2013).

Intermittent joints are a prevalent type of discontinuous structural surfaces in engineering rock

masses. The inclination angle and number of joints play a crucial role in the stability of these rock masses. However, there is a lack of systematic discussion on how the angle and number of intermittent joints affect rock mass failure. To address this gap, this paper focuses on fine sandstone, a commonly used rock in engineering. The study involves creating artificial flaws with varying inclinations and numbers in sandstone specimens, which are then subjected to uniaxial compression testing. The rupture process of these flawed specimens is analyzed using acoustic emission technology and digital imaging. By doing so, the study aims to explore the influence of flaw inclination angle and number on the cracking evolution and failure mode of sandstone. The findings of this research can serve as a theoretical reference and provide insights into the failure mechanisms of cracked rock and the development of effective disaster control methods in rock engineering. The research conclusion can be used for blasting, hydraulic fracturing, and rock slopes.

2 Overview of the test

2.1 Test specimen preparation and program

This study focuses on investigating the impact of crack angles and numbers on the failure mode and mechanical properties of rock masses. The research object is intermittent cracks found in engineering rock masses, which are known to contain various types of cracks. The test material used is sandstone, specifically taken from the rock group of hard and relatively hard layered gravel and mudstone interbedded rocks in Zigong City, Sichuan Province. This type of rock is commonly encountered in rock mass engineering and aligns with the engineering background of the analysis and study of destabilization failure in this field. Please refer to Fig. 1 for a visual representation.

The original rock samples were processed into rectangular specimens of thickness \times width \times height of 20 mm \times 50 mm \times 100 mm according to the requirements of the test specification of the International Society of Rock Mechanics (ISRM), with different through-flaws prefabricated in the center of the specimens using the center drilling method, as shown in Fig. 2. The prefabricated flaw consists of four parameters: flaw length a , flaw width d , number of flaws

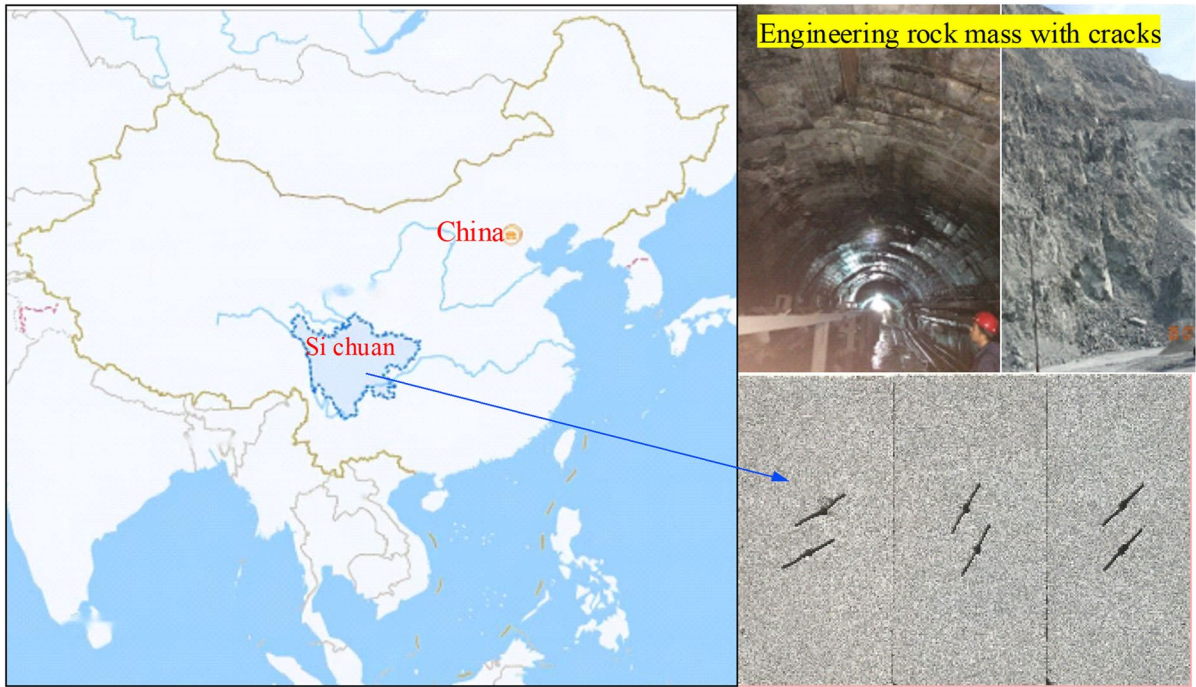


Fig. 1 Sampling location for sandstone samples

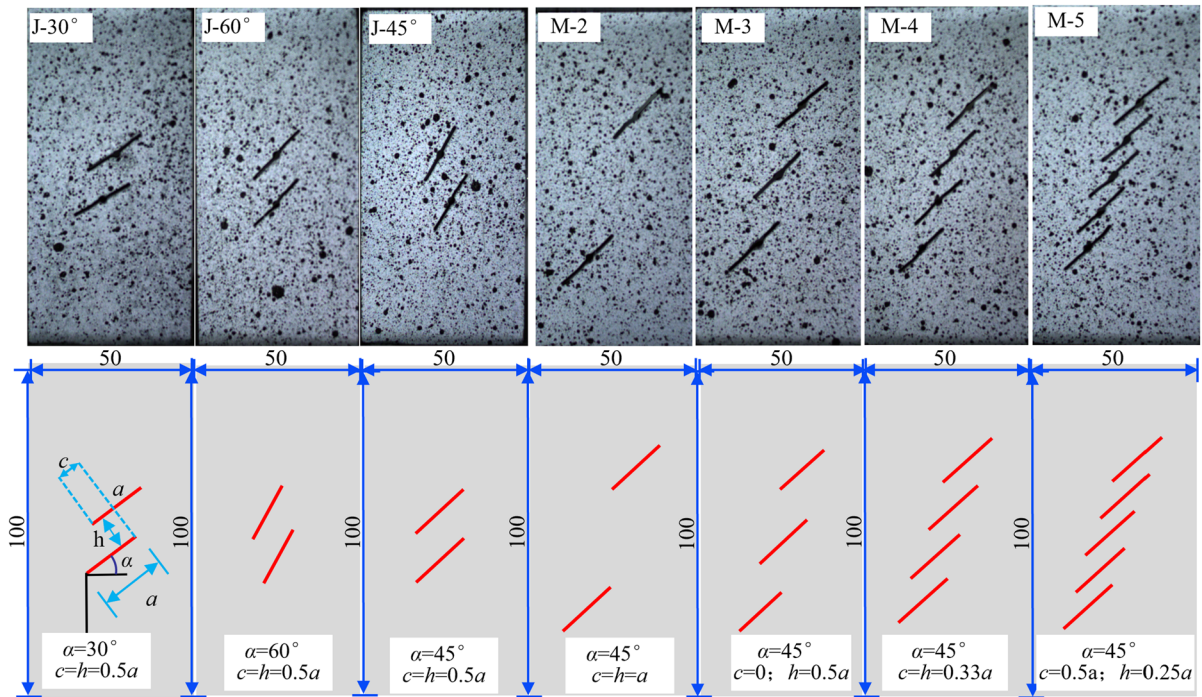


Fig. 2 Prefabricated flaw size of the test specimen (unit: mm)

and flaw inclination α . The flaw length and flaw width were kept constant at $a=20$ mm and $d=1$ mm, respectively. Three flaw inclination types (the angle between the flaw and the horizontal direction) were set up, with inclination angles of 30° , 45° , and 60° , and the corresponding specimen numbers were J- 30° , J- 45° , and J- 60° , respectively. Four different types of flaws were set up, the numbers of which were 2, 3, 4 and 5, and the corresponding specimen numbers were M-2, M-3, M-4 and M-5, respectively; the specific dimensions are shown in Fig. 2. The mechanical parameters of the intact sandstone specimen are average peak strength 89.07Mpa, elastic modulus 8.5GPa Poisson’s ratio 0.26, tensile strength 6.8 MPa, density 2.52×103 kg/m³, wave speed velocity 3624 m/s, and porosity 17%.

2.2 Test system and loading conditions

To ensure controlled variables and minimize experimental errors, the rock specimens were dried at a temperature of 105 °C for 12 h. Before conducting the test, the surface of each specimen was coated with white paint, which was followed by random spraying of black paint after the white paint had completely dried. This spraying process ensured that the paint covered the specimens uniformly and created random scattering spots, which facilitated effective identification during the test. The high-speed camera used for the test had a frame rate of 60 fps. For the uniaxial compression tests on the rock specimens, a

microcontrolled electronic universal testing machine (Changchun Kexin Testing Instrument Co., Ltd., TAW-2000 type) was employed as the loading system. The specimens were loaded based on displacement, with a loading rate of 0.05 mm/min. During compression, the acoustic emission signals from the rock samples were monitored using an acoustic emission monitoring system (Acoustic Physics Corporation PAC, Model PCI-II, USA). To ensure accurate crack observation and minimize the impact of probe arrangement, two probes were positioned on the left and right surfaces of each specimen. The test system and acoustic emission probe arrangement are illustrated in Fig. 3.

3 Influence of the flaw inclination angle on the mechanical properties and failure pattern of specimens

3.1 Stress–strain curves and strength characteristics

Figure 4 presents the load–displacement curves of rock specimens with different flaw inclination angles. The specimens underwent a similar process during loading, which can be roughly divided into four stages: the compaction stage, the elastic stage, the plastic stage, and the failure stage. The compaction stage occurs at the beginning of loading, where the load–displacement curve is typically concave, and the primary cracks within the rock specimen

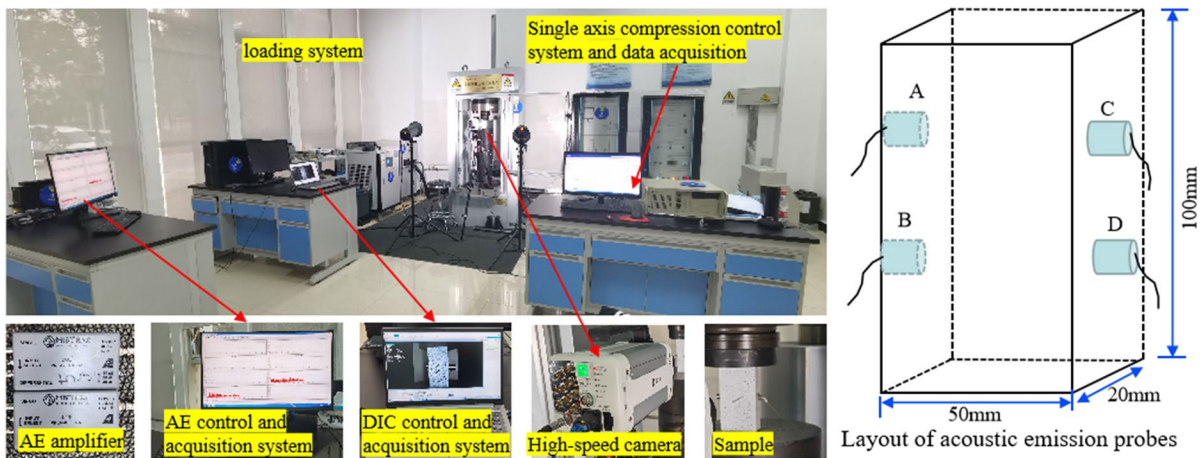


Fig. 3 Principle diagram of the rock mechanics and acoustic emission parameter test system

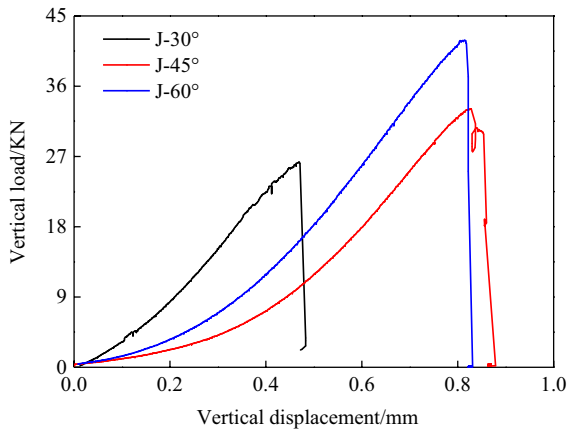


Fig. 4 Load–displacement curves of specimens with different crack angles

close under the applied load. In the elastic stage, the load–displacement curves exhibit a linear variation. The load–displacement curves in the plastic stage show an upward concave pattern, indicating the propagation of cracks within the rock specimen without any macroscopic fracture. Finally, the load displacement curve experiences a vertical drop during the failure stage.

The peak load of the specimen increases as the flaw inclination angle increases. This is because as the flaw inclination angle increases, the rock undergoes a transition from tensile to compressive-shear damage, which gradually strengthens its ability to resist external loads. The load–displacement curves (Fig. 4) show that rock specimens with flaw inclination angles of 45° and 60° experienced significant deformation before final failure, while specimens with a crack inclination angle of 30° experienced minimal deformation before brittle failure. When the flaw inclination angle is greater than 45°, the ductile damage characteristics of the flaw specimen in general with the increase of flaw inclination tends to weaken, which may be due to the fact that when the flaw inclination angle is greater than 45°, the rock structural effect with the increase of flaw inclination is gradually strengthened, which effectively reduces the role of the flaw on the stress concentration of the rock. These findings align with the uniaxial compressive strength law of single crack specimens in rock mechanics (Cai et al. 2002). When the flaw inclination angle reaches 90°, the strength of the rock mass

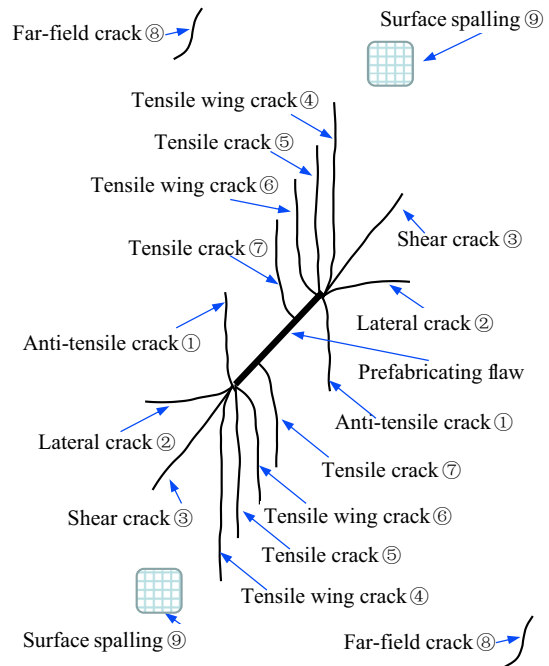


Fig. 5 Nine crack types observed in flawed specimens under uniaxial compression

becomes independent of the flaw, and the strength of the rock mass is solely determined by the rock itself. On the other hand, when the flaw inclination angle is 0°, the rock mass will be destroyed due to lateral propagation of the crack.

3.2 Analysis of the failure characteristics of sandstone specimens

The rock gradually accumulates energy under load and releases it by creating new cracks when it reaches its critical value. The final failure pattern of a rock specimen often depends on the type of crack it produces. Essentially, there are two main types of cracks that occur during the compression failure of rock specimens: tensile or wing cracks and shear or secondary cracks (Bobet 2000). In general, wing cracks appear earlier and are tensile in nature, while secondary cracks appear later and are shear in nature. Literature (Zhou et al. 2019b) categorizes the types of crack propagation under uniaxial compression into nine types, as shown in Fig. 5. A total of seven crack types were observed in this test: tensile wing cracks ④, tensile cracks ⑤, anti-tensile cracks ①, tensile wing

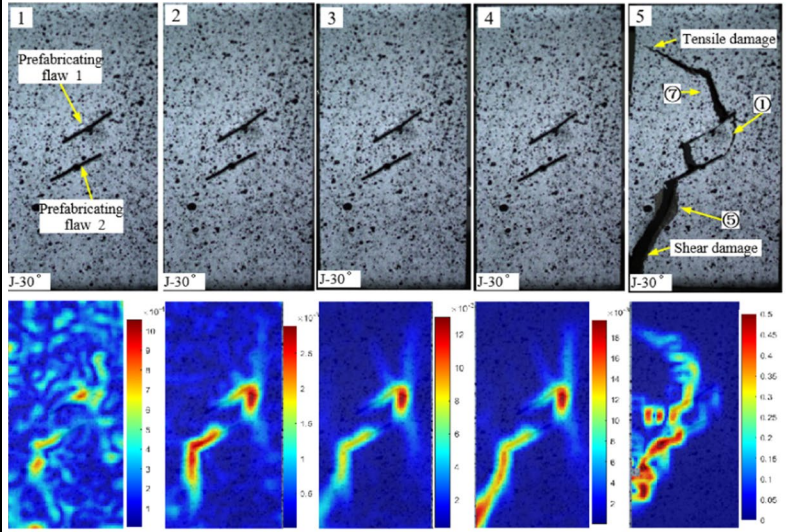
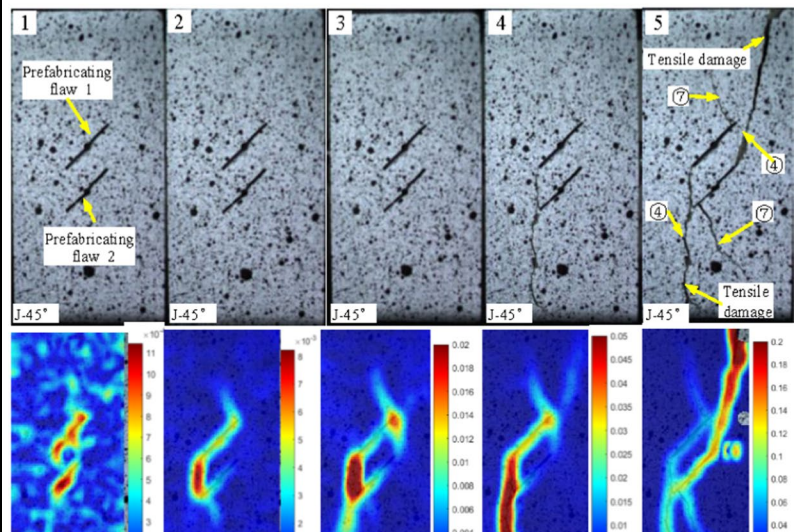
Failure process of sandstone specimen	Description of the failure process of sandstone specimens
 <p style="text-align: center;">(a)</p>	<ol style="list-style-type: none"> 1. Anti-tensile crack ① is generated at the upper tip of prefabricated flaw 1, and tensile wing crack ④ is generated at the lower tip of prefabricated flaw 2. 2. The lower tip of the prefabricated crack 2 produces a Tensile wing crack ④ that propagates continuously. 3. Tensile wing crack ④ keeps propagating downwards, forming a clear strain concentration region, while prefabricated flaw 1 produces tensile crack ⑦. 4. Tensile wing crack ④ generated at the lower tip of prefabricated flaw 2 propagates through the lower end surface of the specimen and shear failure occurs. The anti-tensile crack ① generated at the upper tip of the prefabricated flaw 1 and the upper tip of the prefabricated flaw 2 coalesce. Tensile crack ⑦ generated at the upper tip of prefabricated flaw 1 extends through the left end face of the specimen, and tensile failure occurs.
 <p style="text-align: center;">(b)</p>	<ol style="list-style-type: none"> 1. The lower tip of prefabricated flaw 1 produces a tensile wing crack ④ 2. Tensile wing crack ④ continuously propagates downwards to coalesce with the lower tip of prefabricated flaw 2, while the upper tip of prefabricated flaw 1 and the lower tip of prefabricated law 2 generate tensile wing crack ④. 3. The tensile wing crack generated at the lower tip of the prefabricated flaw 2 propagates downwards, penetrates through the lower section of the specimen, and tensile damage occurs. Tensile crack ⑦ occurs at the upper tip of prefabricated 2. 4. Prefabricated flaw 2 of the upper tip of the tensile wing crack ④ continue to propagate upwards, through the upper end of the specimen, tensile failure occurs, accompanied by tensile crack ⑦ produced, and ultimately the specimen is completely destroyed.

Fig. 6 Damage process of specimens with different crack angles. **a** J-30° sandstone specimen, **b** J-45° sandstone specimen, **c** J-60° sandstone specimen

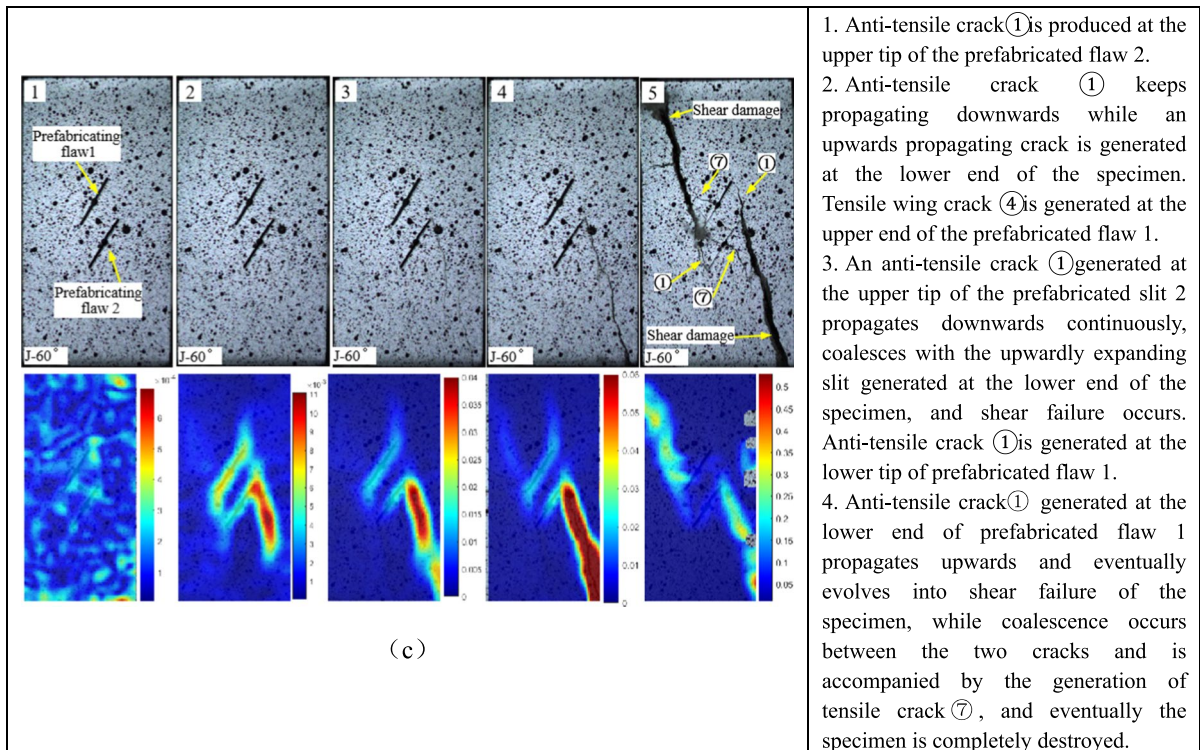


Fig. 6 (continued)

cracks ⑥, tensile cracks ⑦, far-field cracks ⑧, and surface spalling ⑨.

Figure 6 illustrates the development of cracks in the rock specimen influenced by the flaw inclination angle. The cracks are represented by numbers ①~⑨. The analysis of Fig. 6 reveals that the failure of rock specimens is typically a result of multiple crack types occurring simultaneously. For instance, in the case of the J-60° rock specimen, failure characteristics include anti-tensile cracks, tensile wing cracks, and tensile cracks. The failure pattern exhibits clear tensile characteristics. The following summarizes the characteristics of the aforementioned crack types: Among all rock specimens with different flaw inclination angles, tensile cracks are generally the initial crack to appear, with winged tensile cracks being the predominant macroscopic manifestation. However, it is important to note that tensile cracks are often not the ultimate cause of the final failure of the rock specimen. Using the J-30° rock specimen as an example, it can be observed that as stress increases, the development process of the tensile wing crack and anti-tensile crack gradually transforms into secondary shear

cracks. This transformation ultimately leads to the failure of the rock specimen through a combination of tensile and shear forces. Additionally, when the inclination angle of the crack increases, the rock specimen experiences compressive shear failure. This is evident in specimens with an inclination angle of J-60°.

To analyze the crack propagation evolution law of the specimen under different flaw inclination angles in a more detailed manner, the major principal strain field change diagram of the specimen during the loading process is utilized. This analysis provides a fine-grained perspective on the failure process of the specimen, as depicted in Fig. 6. In the case of the J-45° rock specimen, for instance, strain localization initially occurs at the tip of the specimen's prefabricated flaw 2, propagating downwards at an angle. As the stress increases, strain localization becomes more pronounced, leading to visible cracks in the specimen. Although penetration occurs between these cracks, the specimen does not fail. With further loading, the strain concentration band penetrates through the bottom of the specimen, resulting in significant failure. Subsequently, new strain concentration bands

emerge in the specimen, indicated by the appearance of new cracks at a macroscopic level. In essence, the final failure of the specimen is attributed to the continuous accumulation of preexisting damage, with microfractures originating from the tip of the specimen's prefabricated flaws leading to the occurrence of preexisting damage.

3.3 Test results of acoustic emission

The damage of rock is a dynamic process involving internal crack initiation, propagation, and coalescence. The acoustic emission characteristics of rocks are closely related to their internal damage. In order to further investigate the relationship between crack evolution and damage in rock specimens, this section utilizes acoustic emission and photographic monitoring to analyze the damage process in cracked sandstone specimens. Due to the length of the article, only specimen J-30° is analyzed. Figure 7 illustrates the relationship between load, AE counts, and cumulative

AE counts over time during loading of the specimen. Figure 6 (No. J-30°) displays the evolution of macroscopic cracks on the surface of the specimen. In Fig. 7, the black line represents the load, the red line represents the AE counts, the blue line represents the cumulative AE counts, and points 1 to 5 correspond to characteristic points selected based on the load–displacement curves of the specimens, which align with the characteristics of the specimen crack evolution shown in Fig. 6 (No. J-30°).

As illustrated in Fig. 7, the specimen underwent the crack compaction stage and the elastic deformation stage during loading. There were no significant acoustic emission (AE) counts observed between 0 and 270 s, and no visible cracks were observed on the surface of the rock specimens, as shown in Fig. 6 (No. J-30°). The trend of AE cumulative counts in Fig. 7a indicates a gradual increase, suggesting a slow increase in the damage level of the rock specimens. It is important to note that even though no visible cracks formed on the surface of the specimen at this

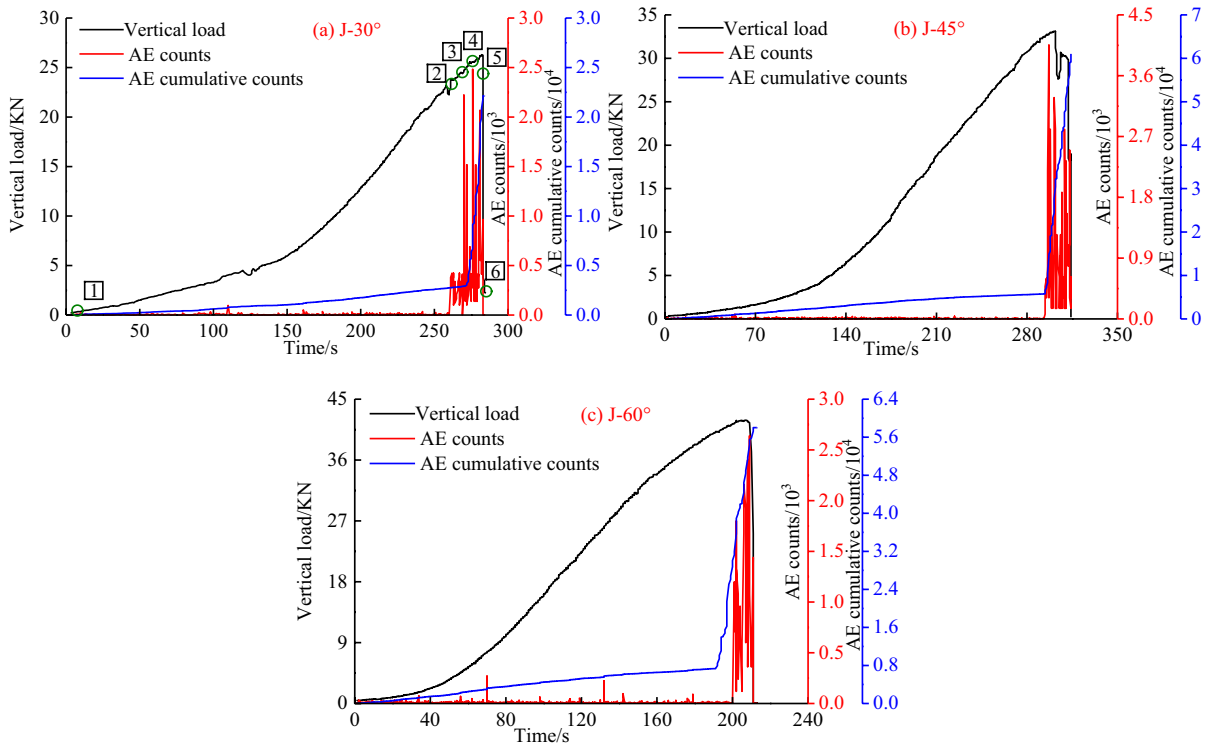


Fig. 7 Acoustic emission test results of specimens with different crack angles. **a** J-30° sandstone specimen, **b** J-45° sandstone specimen, **c** J-60° sandstone specimen

stage, it does not imply that damage failure did not occur internally. Furthermore, Fig. 6 reveals a regular distribution of the strain field and clearly shows areas of stress concentration, indicating the potential for crack initiation and propagation.

With the extension of loading time, the stress–strain curve of the specimen gradually exhibited nonlinear characteristics. Simultaneously, the count value of the AE (acoustic emission) showed an increasing trend, rising from 9 to 367. When the load reached 24.32 MPa (3 points), the rock specimen exhibited its first peak value of AE counts (2487), as depicted in Fig. 7a. At this point, macroscopic cracks formed on the surface of the specimen, and anti-tensile cracks were generated at the tip of the prefabricated flaws, as shown in Fig. 6 (J-30°-3). Subsequently, the AE counts of the specimen entered an 'intense period', with cumulative counts rapidly increasing. This indicated that the damage process of the specimen was accelerated during this stage. The cracks on the surface of the specimen propagated rapidly, generating new cracks, and new anti-tensile cracks formed at the tip of the prefabricated flaws when the stresses reached the 4 points, as shown in Fig. 6 (J-30°-4). When the stress reached point 5, the energy stored in the rock sample reached its critical value, resulting in a sudden drop in stress. This led to the generation of two new shear cracks, as shown in point (J-30°-5) of Fig. 6, ultimately leading to shear failure.

4 Influence of the number of flaws on the mechanical properties and failure pattern of specimens

4.1 Stress–strain curves and strength characteristics

Figure 8a presents the load–displacement curves of specimens with varying numbers of flaws. The loading stages of the specimens are similar and can be categorized into four stages: compression-tightening, elasticity, plasticity, and failure. As shown in Fig. 8a, rock specimens with 4 and 5 flaws exhibited minimal deformations prior to failure, while the rock specimen with 2 flaws underwent significant deformations before failure. The number of cracks in the specimen increased from 2 to 5, leading to a decrease in vertical displacement of the rock from 1.05 to 0.4 mm. Consequently, the rock's ability to withstand external loads gradually diminished.

Figure 8b illustrates that the peak load of the rock mass decreases as the number of flaws in the specimen increases. Specifically, the peak load decreased by 34.5% when the number of flaws changed from 2 to 4. However, as the number of flaws continued to increase, the rate of reduction of the peak load slowed down. For instance, the peak strength was reduced by 10.4% when the number of flaws changed from 4 to 5. The number of cracks had a lesser impact on the initiation load compared to the peak load. When the number of flaws changed from 2 to 5, there was a 15.7%

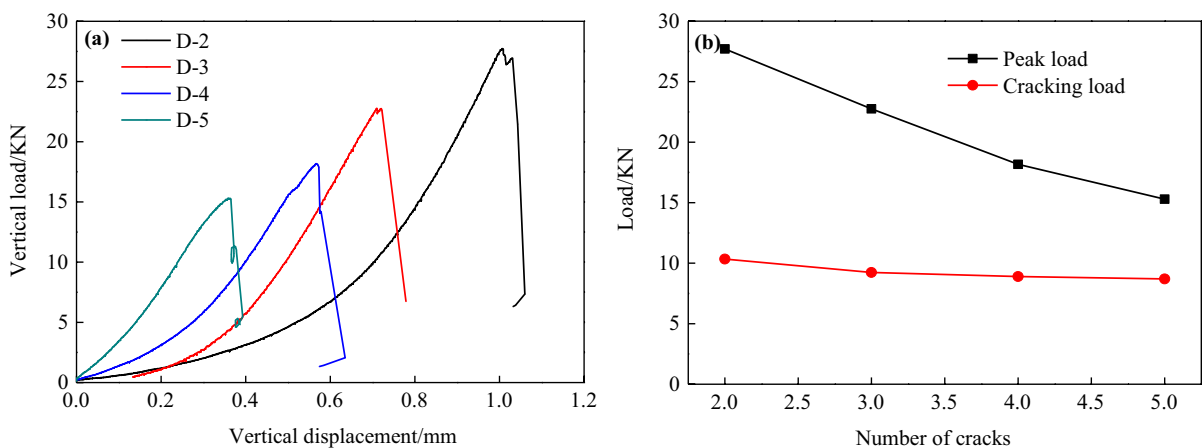


Fig. 8 **a** Load–displacement curves of specimens with different crack numbers, **b** relationship between specimen strength and number of cracks

reduction in the initiation load. The trend of the curve for the initiation load is similar to that of the peak load, indicating that the effect of an increasing number of flaws on the initiation load becomes less significant over time, ultimately leading to a stabilization of the initiation load of the flaws in the specimen.

Literature (Zhu et al. 2002) applied fracture mechanics to derive the propagation length of the wing crack under uniaxial stress. Considering the interaction between the crack and introducing the interaction factor F_1 , the extension length l of the secondary crack is:

$$l = \frac{6.073T^2}{\pi K_{IC}^2} F_1^2 \quad (1)$$

where F_1 is the interaction factor between the cracks, K_{IC} is the critical stress intensity factor, and T is the force on the open (Type I) crack.

$$T = aF_n \sin \theta \quad (2)$$

$$F_n = |\sigma_1 \sin \beta \cos \beta| - f_j \sigma_n - C_j \quad (3)$$

where $\sigma_n = \sigma_1 \sin^2 \beta$, the compressive stress is specified to be positive and the tensile stress is negative, F_n is the crack surface force, σ_n is the crack normal force, and f_j and C_j are the friction coefficient and cohesion of the crack surface, respectively.

The increase in the number of cracks is actually a decrease in the crack spacing h , while the limiting length of crack propagation is:

$$l_m \leq \frac{h}{\sin \beta} \quad (4)$$

From Eq. (4), it can be seen that the increase in the number of cracks is actually a decrease in the ultimate propagation length of the winged cracks under the condition of a constant crack inclination angle, so the cracked rock mass can produce through damage under lower compressive stress, resulting in the reduction of bearing capacity.

4.2 Analysis of the failure characteristics of sandstone specimens

As depicted in Fig. 9, when the number of flaws is small (e.g., D-2), the flaws primarily propagate through tensile wing cracks. These cracks form on

both ends of the prefabricated flaws and initially propagate at an angle of approximately 0° to 20° to the compressive stress. Subsequently, the branch cracks bend and align parallel to the direction of the compressive stress. During this stage, as the tensile stress field dominates, the cracks mainly propagate under the influence of tensile stress, following a tensile mode of propagation. Due to the relatively wide spacing between the flaws, the tensile wing crack resulting from the propagation of the two cracks continues along the direction of the compressive stress until it penetrates through the entire specimen, causing penetration damage between the prefabricated flaw and the tensile wing crack.

As the number of cracks increases, the outer two prefabricated flaws generate tensile wing cracks when subjected to tensile stress and propagate in the direction of compressive stress. The stress field of the rock bridge section between the two outer prefabricated flaws gradually transitions from a tensile stress field to a compressive stress field due to the interaction between the prefabricated flaws. This means that the inner prefabricated flaws experience high pressure stress and undergo pressure-shear damage, causing the propagation of their cracks to be suppressed by the compressive stress field. The damage is manifested as the absence of tip cracks in the inner prefabricated flaw. The destruction of the entire specimen occurs along the direction of tensile wing crack of the outer prefabricated flaw and the inner prefabricated flaw. Moreover, as the number of prefabricated flaws increases, the angle at which fracture propagation begins gradually increases, transitioning from a direction roughly parallel to the compressive stress to a direction perpendicular to the prefabricated flaws. When the density of the prefabricated flaws is increased, the specimens exhibit resistance to tensile crack propagation, as observed in D-4 and D-5.

4.3 Test results of acoustic emission

According to Fig. 10, the rock initially exhibited weak AE counts and low cumulative AE counts before the specimen failed. However, a sudden increase in AE counts occurred, which accounted for a significant portion of the total AE energy. Subsequently, the

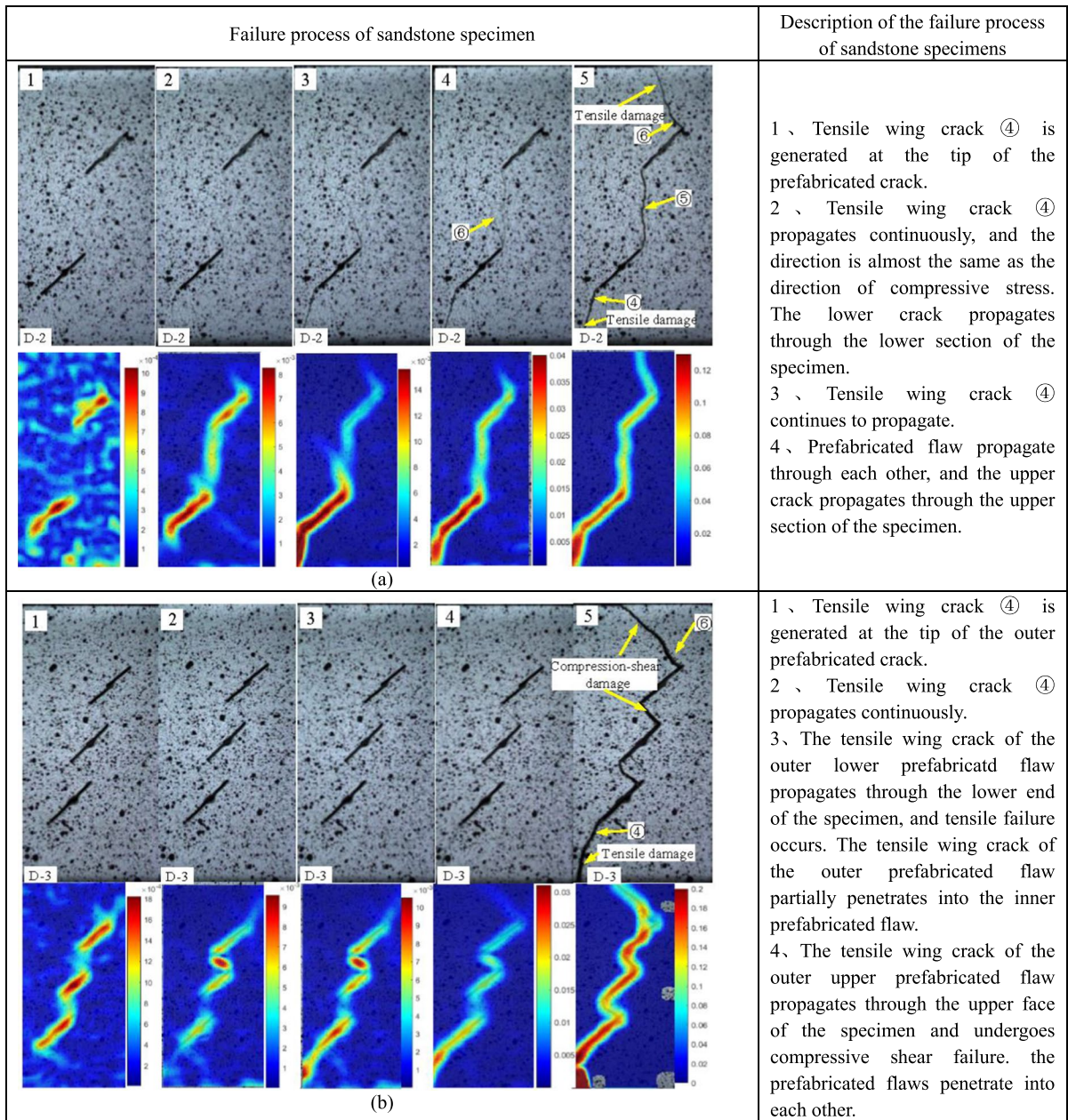
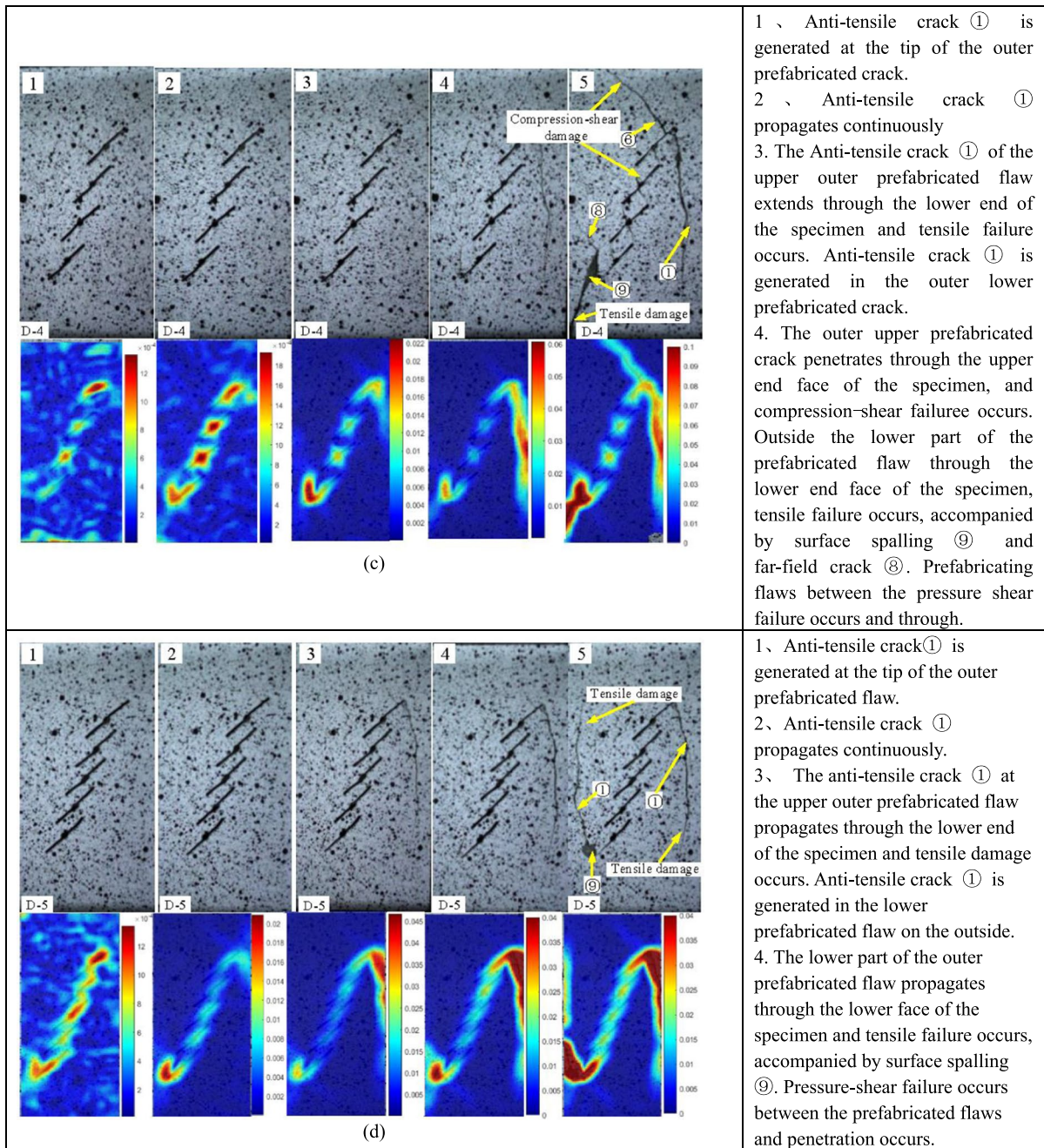


Fig. 9 Damage process of specimens with different crack numbers. **a** D-2 sandstone specimen, **b** D-3 sandstone specimen, **c** D-4 sandstone specimen, **d** D-5 sandstone specimen



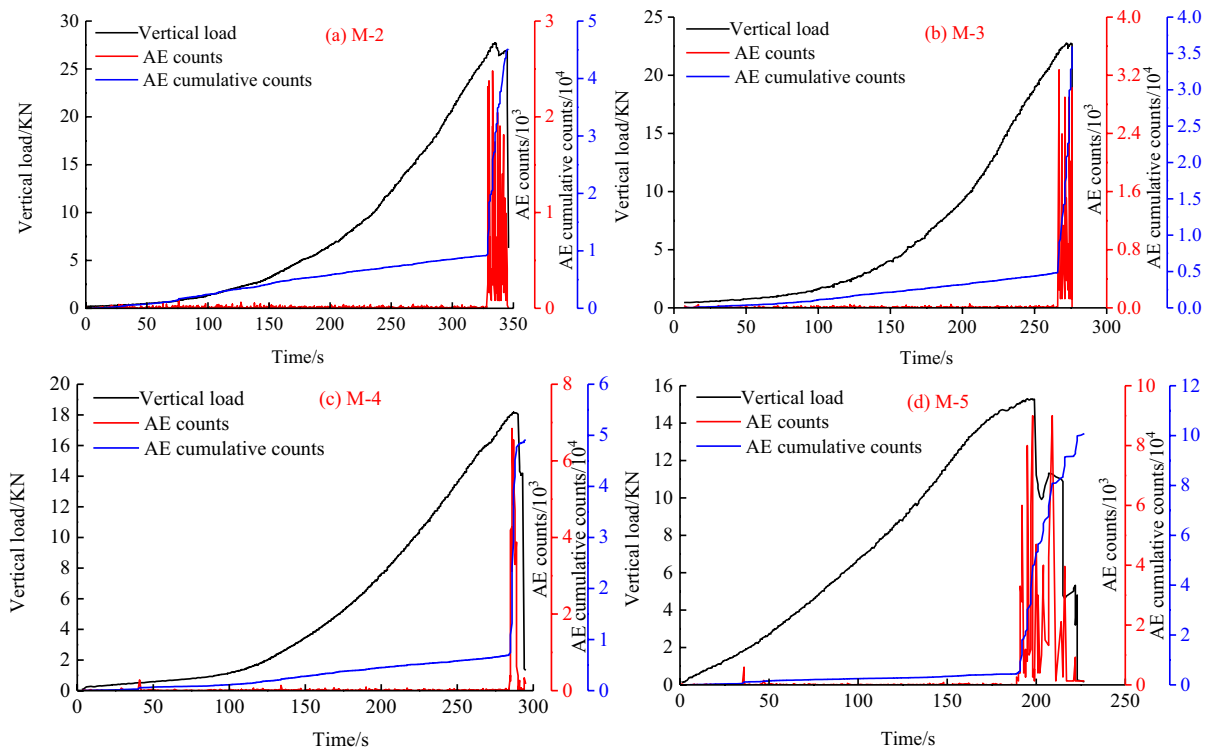


Fig. 10 Acoustic emission test results of specimens with different crack numbers. **a** D-2 sandstone specimen, **b** D-3 sandstone specimen, **c** D-4 sandstone specimen, **d** D-5 sandstone specimen

value of AE counts under uniaxial compression did not increase linearly with the number of prefabricated flaws, as it was influenced by crack development and microfracture generation. However, the cumulative value of AE counts increased with an increase in the number of prefabricated flaws. This relationship can serve as a theoretical basis for future assessments of crack propagation during rock mass failure and the relative sizes of prefabricated flaws in specimens.

5 Discussion

To further investigate the mechanical process of crack propagation, the theory of fracture mechanics is employed to examine the pattern of crack initiation. A mechanical model of crack propagation was created using the uniaxial force diagram of the specimen depicted in Fig. 11. The fracture penetration mode of the sandstone specimen was analyzed. In this model, the axial stress is denoted as σ_1 , and the angle

between the inclined cleavage and the maximum principal plane is α . The axial stress σ_1 is divided into the tangential stress τ_n and the normal stress σ_n at the inclined crack surface, which can be expressed as follows:

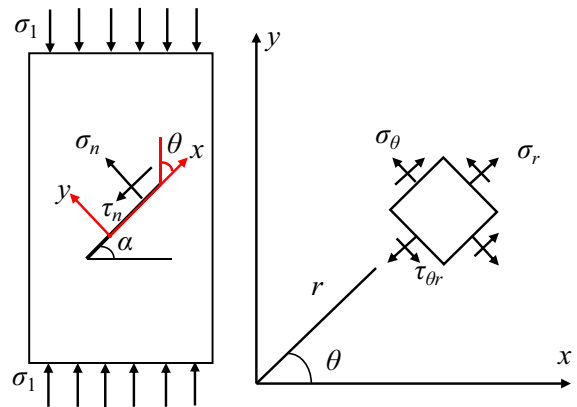


Fig. 11 Mechanical model of crack propagation

$$\begin{cases} \sigma_n = \sigma_1 \cos^2 \alpha \\ \tau_n = \frac{\sigma_1}{2} \sin 2\alpha \end{cases} \quad (5)$$

In Eq. (5), $\sigma_n > 0$, the force acting on the inclined crack surface behaves as a tensile stress; $\sigma_n < 0$, as a compressive stress. A two-dimensional fracture mechanics analysis of the cracks in the specimen is performed by considering the specimen profile as an infinite-body planar problem containing cracks of length $2a$. The specimen is unidirectionally pressurized and is more significantly affected by the boundary, and the stress intensity factor at the tip of the crack is approximated as (Li et al. 2005b):

$$\begin{cases} K_I = \sigma_1 \sqrt{\pi a} \cos^2 \alpha \\ K_{II} = \sigma_1 \sqrt{\pi a} \cos \alpha \sin \alpha \end{cases} \quad (6)$$

where K_I is the type I fracture stress intensity factor and K_{II} is the type II fracture stress intensity factor.

The stress component in polar coordinates for a type I and II composite crack, as shown in Fig. 11, can be expressed as:

$$\begin{cases} \sigma_r = \frac{1}{2\sqrt{2\pi r}} \left[K_I(3 - \cos \theta) \cos \frac{\theta}{2} + K_{II}(3 \cos \theta - 1) \sin \frac{\theta}{2} \right] \\ \sigma_\theta = \frac{1}{2\sqrt{2\pi r}} \cos \frac{\theta}{2} \left[K_I(1 + \cos \theta) - 3K_{II} \sin \theta \right] \\ \tau_{r\theta} = \frac{1}{2\sqrt{2\pi r}} \cos \frac{\theta}{2} \left[K_I \sin \theta + K_{II}(3 \cos \theta - 1) \right] \end{cases} \quad (7)$$

According to the maximum circumferential tensile stress criterion, the crack initiates and propagates along the direction where the circumferential stress σ_θ

is maximum, and the direction of initiation satisfies the following condition:

$$\frac{\partial \sigma_\theta}{\partial \theta} = 0 \quad \frac{\partial^2 \sigma_\theta}{\partial \sigma_\theta^2} = 0 \quad (8)$$

Substituting Eq. (3) into Eq. (4) and setting $\partial \sigma_\theta / \sigma_\theta = 0$, the calculation result can be expressed as:

$$K_I \sin \theta_0 + 3K_{II}(3 \cos \theta_0 - 1) = 0 \quad (9)$$

When $\sigma_{\theta_{max}} = \sigma_{\theta_c}$, the crack starts to initiate and propagate. σ_{θ_c} is the maximum circumferential stress critical value, and σ_{θ_c} can be determined by the fracture toughness K_{Ic} of the type I crack to be $\sigma_{\theta_c} = K_{Ic} / \sqrt{2\pi r}$. Combined with Eq. (3), it can be further determined that the fracture criterion of the composite crack of type I, II is:

$$\cos \frac{\theta_0}{2} \left[K_I \cos^2 \frac{\theta_0}{2} - \frac{3}{2} K_{II} \sin \theta_0 \right] = K_{Ic} \quad (10)$$

The approximate values of K_I and K_{II} are:

$$\begin{cases} K_I = \frac{1}{2} \sigma_1 \sqrt{\pi a} \sin \alpha \\ K_{II} = \frac{1}{2} \sigma_1 \sqrt{\pi a} \cos \alpha \end{cases} \quad (11)$$

As shown in the model in Fig. 11, the crack initiation angle at the tip of an inclined crack can be calculated from the crack tip stress intensity factor and combined with the maximum circumferential stress criterion. K_I and K_{II} are calculated by bringing α into Eq. (11), following which the angle of initiation of the crack, θ_0 , can be calculated by bringing α into Eq. (9). As shown in Table 1 for the theoretical

Table 1 Theoretical value and test comparison of the crack initiation angle

Type	Specimen No	Actual crack initiation angle of the flaw θ_0 (°)	Theoretical calculation of crack initiation angle of the flaw θ_s (°)
Different flaw angles	J-30°	34.7	36.7
	J-45°	46.6	49.8
	J-60°	61.8	66.5
Different number of flaws	M-2	42.6	51.8
	M-3	37.8	41.3
	M-4	53.8	56.7
	M-5	49.5	55.1

value of the crack initiation angle and the test value comparison results, the theoretical calculation results and test results are in the error base allowable range, which further verifies the feasibility and reasonableness of the theoretical calculation results in this paper.

This study reveals that the destruction of the rock mass occurs due to the movement and opening of the original crack surface, leading to the formation of wing-type cracks. These wing-type cracks intersect with primary cracks, creating a network of interconnected cracks in the surrounding rock. This results in significant deformation of the rock mass. If the wing crack does not propagate up to its maximum length, it indicates the absence of a perimeter rock fracture zone. Therefore, the boundary of intermittent fracture penetration failure can be defined as the boundary of the perimeter rock rupture zone. In this zone, primary cracks and wing cracks intersect, and the rock mass is weakened due to the penetration of these cracks. If the winged cracks of adjacent cracks are not penetrated, it suggests that the rock mass still possesses high strength but has reached its limit state and will quickly undergo destruction, although it can still withstand high loads. Since the majority of the rock formation in the roadway area is characterized by intermittent cracks, the boundary of intermittent crack penetration failure can be considered as a universal and general definition.

6 Conclusions

Fractured rock mass is a highly intricate medium characterized by strong non-uniformity and nonlinearity. It contains intersecting crack defects of various scales that significantly influence its physical and mechanical properties. Additionally, in engineering applications, rocks are subject to dynamic disturbances like earthquakes, blasting vibrations, and excavation activities, which can lead to the formation of interconnected cracks and trigger geological disasters. This study focuses on the fabrication of sandstone into diverse fractured rock samples for subsequent uniaxial compression and acoustic emission experiments. By analyzing fracture mechanics and acoustic emission characteristics, the research delves into the crack initiation mechanisms of fractured rock masses. The conclusion is as follows:

1. The displacement and peak load of the specimens decreased as the number of cracks increased. The increase in the number of flaws reduces the ultimate propagation length of the wing crack, leading to through failure and a reduced load carrying capacity of the specimen at lower compressive stresses.
2. As the inclination angle of the flaw increases, the failure mode of the specimen transitions from shear to compressive failure. During the initial stage of loading, a high-strain region emerges around the flaw. As loading continues, a localized high-strain region develops on the surface of the specimen, indicating the path along which a macroscopic crack may form.
3. When there are only a few flaws, the flaws primarily spread through tensile wing cracks. As the number of flaws increases, the inner flaw does not generate tip cracks. Instead, the failure of the entire specimen occurs along the direction of the tensile wing crack of the outer prefabricated flaw, with the inner flaw extending through the specimen, resulting in an anti-tensile crack.
4. Among the rock specimens with all flaw inclination angles, the winged tensile crack was the first crack to appear. Based on the principle of fracture mechanics, the expression of the stress intensity factor at the tip of the crack under uniaxial compression conditions without considering the closure effect was given, the crack initiation angle was calculated, and the theoretical calculation of the initiation angle was basically consistent with the test results.

Author contributions Conceptualization, J.P. (Jiewen Pang) and Q.H. (Qiaoyun Han); funding acquisition, J.P. (Jiewen Pang) and X.S. (Xiaoyuan Sun); methodology, J.P. (Jiewen Pang) and D.B. (Deyang Ba); writing—original draft, J.P. (Jiewen Pang); writing—review and editing, Y.H. (Yongliang He).

Funding This research was funded by the National Natural Science Foundation of China (42202321), by the Scientific and Technological Innovation Programs of Higher Education Institutions in Shanxi (2019L0641), by the Fundamental Research Program of Shanxi Province (202103021224277, 202203021222184), and by the Taiyuan University of Science and Technology Scientific Research Initial Funding (20222112).

Data availability Data will be made available on request.

Declarations

Conflict of interest The authors declare that they have no known competing financial interests or personal relationships that could have appeared to influence the work reported in this paper.

Ethics approval Not applicable, Ethics approval was not required for this research.

Consent to publish All authors agreed to publish.

Open Access This article is licensed under a Creative Commons Attribution 4.0 International License, which permits use, sharing, adaptation, distribution and reproduction in any medium or format, as long as you give appropriate credit to the original author(s) and the source, provide a link to the Creative Commons licence, and indicate if changes were made. The images or other third party material in this article are included in the article's Creative Commons licence, unless indicated otherwise in a credit line to the material. If material is not included in the article's Creative Commons licence and your intended use is not permitted by statutory regulation or exceeds the permitted use, you will need to obtain permission directly from the copyright holder. To view a copy of this licence, visit <http://creativecommons.org/licenses/by/4.0/>.

References

- Abdollahipour A, Marji MF (2020) A thermo-hydromechanical displacement discontinuity method to model fractures in high-pressure, high-temperature environments. *Renew Energy* 153:1488–1503. <https://doi.org/10.1016/j.renene.2020.02.110>
- Abdollahipour A, Fatehi Marji M, Yarahmadi Bafghi AR, Gholamnejad J (2016) Numerical investigation of effect of crack geometrical parameters on hydraulic fracturing process of hydrocarbon reservoirs. *J Min Environ* 7(2):205–214
- Alneasan M, Behnia M (2022) Analytical and experimental investigation on the effect of loading rate on the fracture toughness and fracture envelope in brittle rocks. *Theor Appl Fract Mech* 119:103300. <https://doi.org/10.1016/j.tafmec.2022.103300>
- Alneasan M, Behnia M, Alzo'ubi AK (2022) Experimental observations on the effect of strain rate on rock tensile fracturing. *Int J Rock Mech Min Sci* 160:105256. <https://doi.org/10.1016/j.ijrmms.2022.105256>
- Alneasan M, Alzo'ubi AK, Okasha N (2023) A comprehensive study for the effect of sample geometry and lateral pressure on shear fractures using the short core in compression (SCC) method. *Eur J Mech A/Solids* 100:104988. <https://doi.org/10.1016/j.euromechsol.2023.104988>
- Bobet A (2000) The initiation of secondary cracks in compression. *Eng Fract Mech* 66:187–219. [https://doi.org/10.1016/S0013-7944\(00\)00009-6](https://doi.org/10.1016/S0013-7944(00)00009-6)
- Bobet A, Einstein HH (1998) Fracture coalescence in rock-type materials under uniaxial and biaxial compression. *Int J Rock Mech Min Sci* 35:863–888. [https://doi.org/10.1016/S0148-9062\(98\)00005-9](https://doi.org/10.1016/S0148-9062(98)00005-9)
- Cai MF, He MC, Liu DY (2002) Rock mechanics and engineering. Science Press, Beijing, pp 104–108
- Cao P, Liu T, Pu C, Lin H (2015) Crack propagation and coalescence of brittle rock-like specimens with preexisting cracks in compression. *Eng Geol* 187:113–121. <https://doi.org/10.1016/j.enggeo.2014.12.010>
- Chang X, Deng Y, Li Z, Wang S, Tang CA (2018) Crack propagation from a filled flaw in rocks considering the infill influences. *J Appl Geophys* 152:137–149. <https://doi.org/10.1016/j.jappgeo.2018.03.018>
- Debecker B, Vervoort A (2013) Two-dimensional discrete element simulations of the fracture behaviour of slate. *Int J Rock Mech Min Sci* 61:161–170. <https://doi.org/10.1016/j.ijrmms.2013.02.004>
- Eberhardt E, Stead D, Stimpson B, Read RS (1998) Identifying crack initiation and propagation thresholds in brittle rock. *Can Geotech J* 35:222–233. <https://doi.org/10.1139/t97-091>
- Fu J, Haeri H, Sarfarazi V, Asgari K, Ebneabbasi P, Fatehi Marji M, Guo M (2022) Extended finite element method simulation and experimental test on failure behavior of defects under uniaxial compression. *Mech Adv Mater Struct* 29(27):6966–6981. <https://doi.org/10.1080/15376494.2021.1989730>
- Han W, Jiang Y, Luan H, Du Y, Zhu Y, Liu J (2020) Numerical investigation on the shear behavior of rock-like materials containing fissure-holes with FEM-CZM method. *Comput Geotech* 125:103670. <https://doi.org/10.1016/j.compgeo.2020.103670>
- Hoek E, Bieniawski ZT (1965) Brittle fracture propagation in rock under compression. *Int J Fract* 3:137–155
- Huang S, Yao N, Ye Y, Cui X (2019) Strength and failure characteristics of rocklike material containing a large-opening crack under uniaxial compression: experimental and numerical studies. *Int J Geomech* 19:1–15. [https://doi.org/10.1061/\(asce\)gm.1943-5622.0001477](https://doi.org/10.1061/(asce)gm.1943-5622.0001477)
- Huang X, Shi C, Ruan H, Zhang Y, Zhao W (2022) Stable crack propagation model of rock based on crack strain. *Energies* 15:1–13. <https://doi.org/10.3390/en15051885>
- Ji WW, Pan PZ, Lin Q, Feng XT, Du MP (2016) Do disk-type specimens generate a mode II fracture without confinement? *Int J Rock Mech Min Sci* 87:48–54. <https://doi.org/10.1016/j.ijrmms.2016.05.010>
- Lak M, Marji MF, Bafghi AY, Abdollahipour A (2019a) Analytical and numerical modeling of rock blasting operations using a two-dimensional elasto-dynamic Green's function. *Int J Rock Mech Min Sci* 114:208–217. <https://doi.org/10.1016/j.ijrmms.2018.12.022>
- Lak M, Marji MF, Bafghi AY, Abdollahipour A (2019b) Discrete element modeling of explosion-induced fracture extension in jointed rock masses. *J Min Environ* 10(1):125–138
- Lei R, Zhang Z, Ge Z, Berto F, Wang G, Zhou L (2020) Deformation localization and cracking processes of sandstone

- containing two flaws of different geometric arrangements. *Fatigue Fract Eng Mater Struct* 43:1959–1977. <https://doi.org/10.1111/ffe.13259>
- Li YP, Chen LZ, Wang YH (2005a) Experimental research on precracked marble under compression. *Int J Solids Struct* 42:2505–2516. <https://doi.org/10.1016/j.ijsolstr.2004.09.033>
- Li LY, Xu FG, Gao F, Wang L, Che FX (2005b) Fracture mechanics analysis of rock bridge failure mechanism. *Chin J Rock Mech Eng* 24:4328–4334
- Lin Q, Biolzi L, Labuz JF (2013) Opening and mixed-mode fracture initiation in a quasi-brittle material. *J Eng Mech* 139:177–187. [https://doi.org/10.1061/\(asce\)em.1943-7889.0000488](https://doi.org/10.1061/(asce)em.1943-7889.0000488)
- Liu Q, Xu J, Liu X, Jiang J, Liu B (2015) The role of flaws on crack growth in rock-like material assessed by AE technique. *Int J Fract* 193:99–115. <https://doi.org/10.1007/s10704-015-0021-6>
- Liu X, Wu L, Zhang Y, Wang S, Yao X, Wu X (2021) The characteristics of crack existence and development during rock shear fracturing evolution. *Bull Eng Geol Environ* 80:1671–1682. <https://doi.org/10.1007/s10064-020-01997-3>
- Modiriasari A, Bobet A, Pyrak-Nolte LJ (2017) Active seismic monitoring of crack initiation, propagation, and coalescence in rock. *Rock Mech Rock Eng* 50:2311–2325. <https://doi.org/10.1007/s00603-017-1235-x>
- Mohebbi M, Yarahmadi Bafghi AR, Fatehi Marji M, Gholamnejad J (2017) Rock mass structural data analysis using image processing techniques (Case study: Choghart iron ore mine northern slopes). *J Min Environ* 8(1):61–74
- Morgan SP, Einstein HH (2017) Cracking processes affected by bedding planes in Opalinus shale with flaw pairs. *Eng Fract Mech* 176:213–234. <https://doi.org/10.1016/j.engfractmech.2017.03.003>
- Munoz H, Taheri A (2017) Specimen aspect ratio and progressive field strain development of sandstone under uniaxial compression by three-dimensional digital image correlation. *J Rock Mech Geotech Eng* 9:599–610. <https://doi.org/10.1016/j.jrmge.2017.01.005>
- Reis JML, Nunes LCS, Mattos HSC (2015) Crack propagation analysis of polymer mortars brazilian disc specimens containing cracks under compressive line loading. *Adv Mater Res* 1129:429–437. <https://doi.org/10.4028/www.scientific.net/amr.1129.429>
- Sarfarazi V, Ghazvinian A, Schubert W, Blumel M, Nejati HR (2014) Numerical simulation of the process of fracture of echelon rock joints. *Rock Mech Rock Eng* 47:1355–1371. <https://doi.org/10.1007/s00603-013-0450-3>
- Wang SY, Sloan SW, Sheng DC, Yang SQ, Tang CA (2014) Numerical study of failure behaviour of precracked rock specimens under conventional triaxial compression. *Int J Solids Struct* 51:1132–1148. <https://doi.org/10.1016/j.ijsolstr.2013.12.012>
- Wang Y, Wang Y, Luo S, Liu H, Yi G, Peng K (2023) Influence of the crack angle on the deformation and failure characteristics of sandstone under stepped cyclic uniaxial compression with a constant lower limit. *Mathematics* 11:2187. <https://doi.org/10.3390/math11092187>
- Wong RHC, Lin P (2015) Numerical study of stress distribution and crack coalescence mechanisms of a solid containing multiple holes. *Int J Rock Mech Min Sci* 79:41–54. <https://doi.org/10.1016/j.ijrmms.2015.08.003>
- Yang H, Lin H, Wang Y, Cao R, Li J, Zhao Y (2021) Investigation of the correlation between crack propagation process and the peak strength for the specimen containing a single preexisting flaw made of rock-like material. *Arch Civ Mech Eng*. <https://doi.org/10.1007/s43452-021-00175-w>
- Yang S, Dong J, Yang J, Yang Z, Huang Y (2022) An experimental investigation of failure mechanical behavior in cylindrical granite specimens containing two noncoplanar open fissures under different confining pressures. *J Cent South Univ* 29:1578–1596. <https://doi.org/10.1007/s11771-022-5035-4>
- Zhang JZ, Zhou XP (2020) AE event rate characteristics of flawed granite: from damage stress to ultimate failure. *Geophys J Int* 222:795–814. <https://doi.org/10.1093/gji/ggaa207>
- Zhang JZ, Zhou XP, Zhou LS, Berto F (2019) Progressive failure of brittle rocks with nonisometric flaws: Insights from acousto-optic-mechanical (AOM) data. *Fatigue Fract Eng Mater Struct* 42:1787–1802. <https://doi.org/10.1111/ffe.13019>
- Zhao C, Zhou Y, Zhao C, Bao C (2018) Cracking processes and coalescence modes in rock-like specimens with two parallel preexisting cracks. *Rock Mech Rock Eng* 51:3377–3393. <https://doi.org/10.1007/s00603-018-1525-y>
- Zhou XP, Cheng H, Feng YF (2014) An experimental study of crack coalescence behaviour in rock-like materials containing multiple flaws under uniaxial compression. *Rock Mech Rock Eng* 47:1961–1986. <https://doi.org/10.1007/s00603-013-0511-7>
- Zhou XP, Zhang JZ, Qian QH, Niu Y (2019a) Experimental investigation of progressive cracking processes in granite under uniaxial loading using digital imaging and AE techniques. *J Struct Geol* 126:129–145. <https://doi.org/10.1016/j.jsg.2019.06.003>
- Zhou XP, Niu Y, Zhang JZ, Shen XC, Zheng Y, Berto F (2019b) Experimental study on effects of freeze-thaw fatigue damage on the cracking behaviors of sandstone containing two unparallel fissures. *Fatigue Fract Eng Mater Struct* 42:1322–1340. <https://doi.org/10.1111/ffe.12987>
- Zhu WS, Li SC, Chen WZ (2002) Failure mechanism and anchoring effect of jointed rock masses and engineering applications. Science Press, Beijing, pp 73–75

Publisher's Note Springer Nature remains neutral with regard to jurisdictional claims in published maps and institutional affiliations.